Electronic Supplementary Material (ESI) for Energy Advances.


# Evaluation of binderless LTA and SAPO-34 beads as $CO_2$ adsorbents for biogas upgrading in a Vacuum Pressure Swing Adsorption setup

Dina G. Boer,[a,b] Henk H. van de Bovenkamp,[a] Jort Langerak,[b] Benny Bakker,[b] Paolo P. Pescarmona[a,*]

[a] Chemical Engineering Group, Engineering and Technology Institute Groningen (ENTEG), Faculty of Science and Engineering, University of Groningen, Nijenborgh 4, 9747 AG , Groningen, The Netherlands

[b] DMT Environmental Technology, Yndustrywei 3, 8501 SN, Joure, The Netherlands;

*Corresponding author: p.p.pescarmona@rug.nl

## Supplementary information

*Figure S1: Experimental setup used in this work for conducting the breakthrough experiments.*

## Theory of breakthrough experiments

The feed concentration at the inlet of the column, typically 40% $CO_2$ and 60% $CH_4$ for biogas, is denoted as $C_0$. Before the start of the adsorption, the $CO_2$ concentration (C) in the column is 0% at t = 0 (Figure S2, column A). Then, at the start of the experiment, the $CO_2/CH_4$ feed is led through the column, and $CO_2$ is selectively adsorbed on the adsorbent bed (Figure S2, column B to D). This means that the mixture that reaches the IR sensor will contain (nearly) no $CO_2$ ($C/C_0 \approx 0$). The section of the bed in which $CO_2$ is adsorbed is called the mass transfer zone (in green in the scheme in the columns in Fig. 2). As time progresses, the bottom of the bed becomes saturated with adsorbate (i.e. at equilibrium with the inlet gas stream, zone in dark grey from column C on) and the mass transfer zone progresses along the column (Figure S2, columns C and D). Eventually, the mass transfer zone will reach the outlet of the column and consequently the $CO_2$ concentration in the outlet start to increase. This event is called breakthrough and occurs at the breakthrough time, $t_b$ (Figure S2, column E) [18]. Generally, a concentration of $C/C_0 = 0.05$ is used to define the start of the breakthrough. At this stage, the volume of the mass transfer zone starts to decrease and is considered to have disappeared at $C/C_0 \geq 0.95$ (column F) [19,20]. When this concentration is reached, the adsorbent bed has reached equilibrium with the inlet gas stream and the column is thus considered to be saturated.

The regeneration of the column is typically started at the breakthrough (thus at stage E), as continuing the adsorption would decrease the purity of $CH_4$ in the outlet gas stream. To further increase the purity, a lower breakthrough concentration can be used.

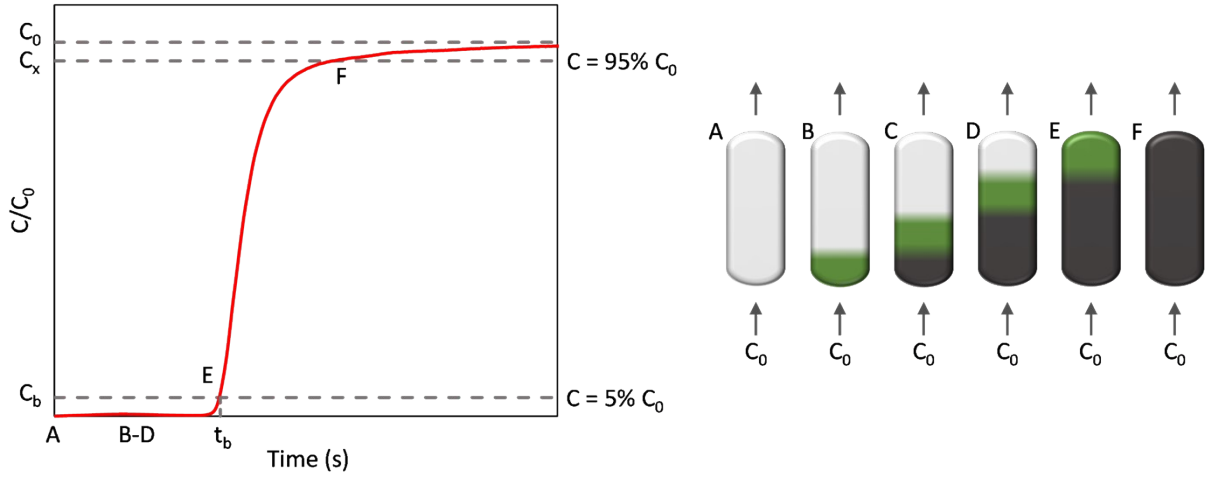


*Figure S2: Breakthrough curve of $CO_2$ from a $CO_2/CH_4$ mixture. At t = 0, the $CO_2$ concentration in the column is 0%, thus the full bed is unused (light grey) (A). As the $CO_2/CH_4$ mixture is led through the bed, $CO_2$ is adsorbed in the mass transfer zone (green) and the rest of the column is still unused (B). The bottom of the bed becomes saturated (dark grey) as the mass transfer zone progresses along the column (C, D). At the breakthrough time ($t_b$), the mass transfer zone reaches the outlet of the column (E). Finally, the bed is completely saturated and the outlet concentration approaches $C_0$ ($C/C_0 \geq 0.95$, F).*

In an ideal adsorption column, the mass transfer is instantaneous, leading to an infinitesimal mass transfer zone (i.e. the mass transfer zone moves through the column as an ideal plug flow) and the breakthrough curve is a step function (Figure S3A) [18]. In practice, mass transfer is not instantaneous, leading to a mass transfer zone in the adsorbent column, and to an S-shaped breakthrough curve (Figure S2 and Figure S3B). The mass transfer rate determines the length of the mass-transfer zone and, therefore, the steepness of the breakthrough curve [18]. A short mass transfer zone is desired in order to achieve high utilization of the adsorbent bed.

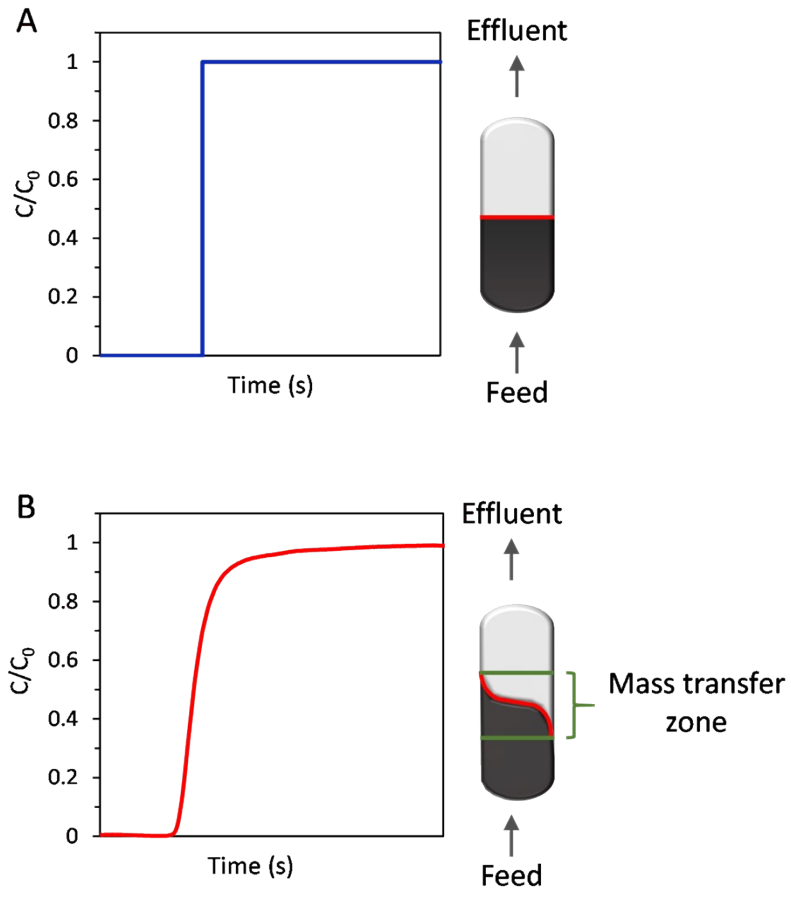


*Figure S3: Ideal adsorption column with instantaneous mass transfer (A); practical adsorption column with a mass transfer zone and an s-shaped breakthrough curve (B).*

## Technical advices for future work

In the breakthrough curves of the adsorbents, a certain amount of tailing is expected as the mass transfer is not instantaneous. However, even in the breakthrough curves obtained with glass beads, in which no $CO_2$ is adsorbed, a tail was observed in the breakthrough curve (Figures S5-S10). This was attributed to the IR measurement, as the IR sensor measures the gas from a small reservoir above the sensor (Figure S4). Since a relatively low gas flow rate (18.2 ml $min^{-1}$) was used in the experiments, and the volume of the reservoir was relatively large, small changes in the gas inlet could not be accurately measured, hence leading to tailing in the breakthrough curves. This tailing should decrease if the volume of the reservoir above the IR sensor were decreased. Another possibility would be to use an online mass spectrometer (MS) or a gas chromatograph (GC) with a thermal conductivity detector (TCD) instead of the IR sensor. An MS would be preferred as the measuring time of a GC is significantly longer than with an MS or IR. Additionally, it could be desirable to measure not only the $CO_2$ concentration but also the $CH_4$ concentration of the outlet gas stream to determine the $CH_4$ breakthrough curves. This could be achieved by adding an additional IR sensor for $CH_4$ to the setup or by using an MS or TCD-GC instead of the IR sensors. Furthermore, it could be interesting to add IR sensors for $CO_2$ and $CH_4$ after the vacuum pump, to determine the concentration of both gases upon desorption. In particular, this would allow determining the purity of the $CO_2$-rich gas stream and the recovery of $CO_2$.

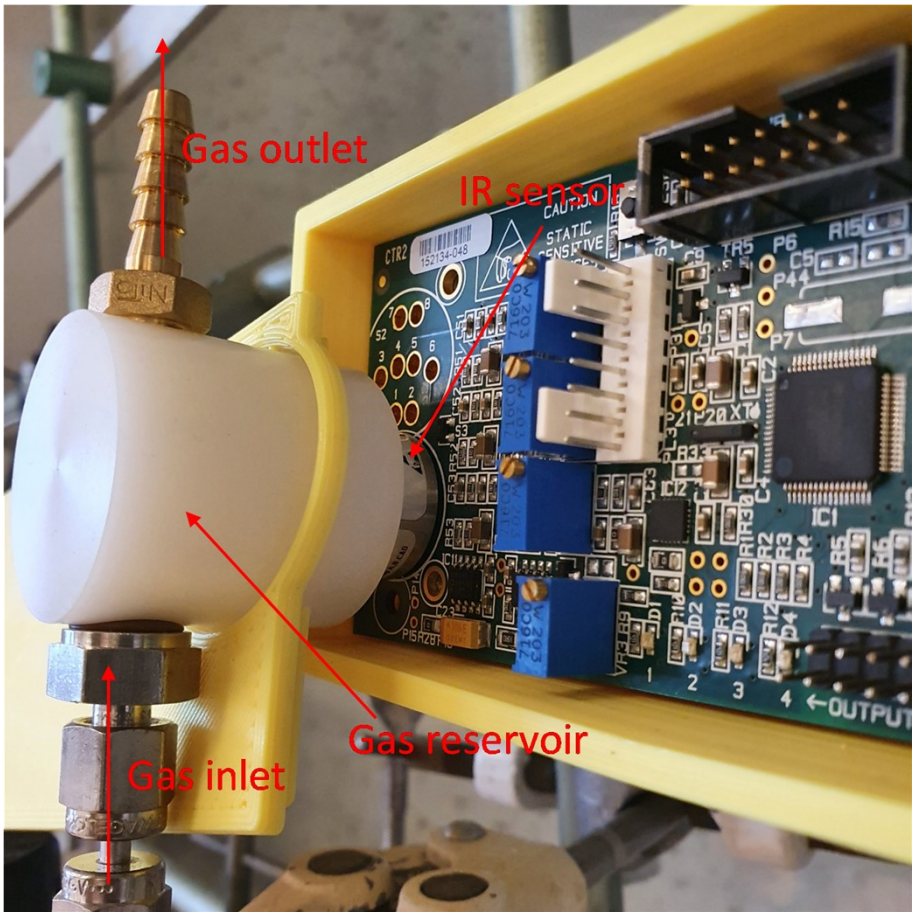


*Figure S4: IR measurement setup. The IR sensor measures the gas from the small gas reservoir attached above the sensor. Although the absorption measured by the IR sensor vs. the gas concentration is not linear, the sensor was internally calibrated at the factory, which allowed us to use a dual-point calibration with our known gas mixtures leading to a linear response.*

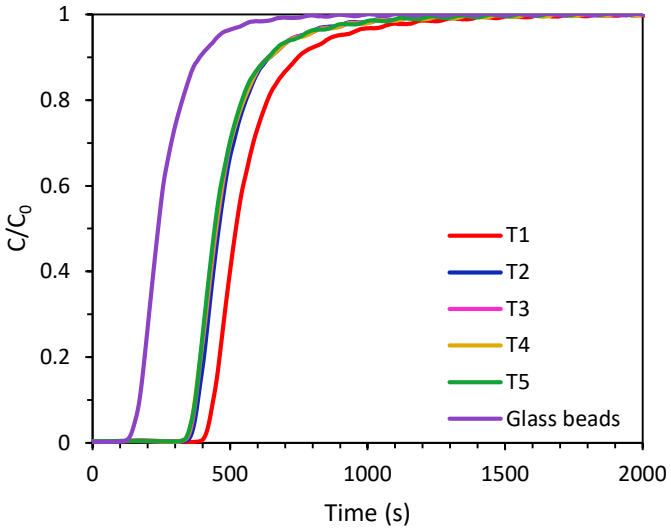


*Figure S5: Cyclic breakthrough curves of LTA beads and glass beads of approximately the same diameter (0.5 mm). LTA beads were regenerated in between cycles by evacuation at 20 mbar for 2 min, followed by flushing with $N_2$ until $CO_2$ concentration ≤ 0.15 %.*

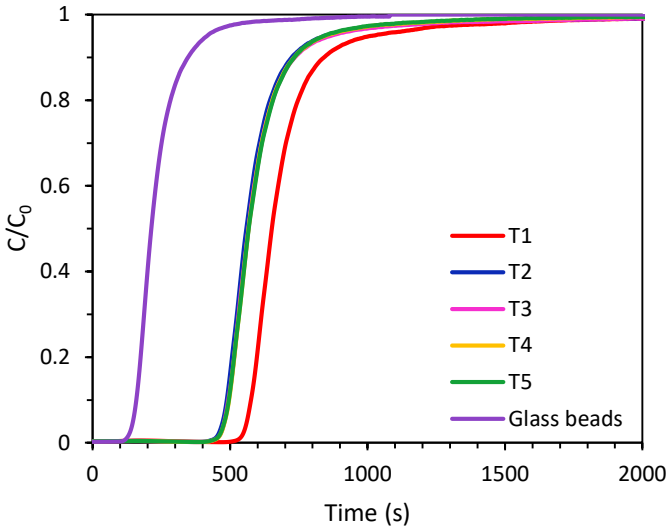


*Figure S6: Cyclic breakthrough curves of the 4A-comm beads and glass beads of approximately the same diameter (3 mm). The 4A-comm beads were regenerated in between cycles by evacuation at 20 mbar for 2 min, followed by flushing with $N_2$ until $CO_2$ concentration ≤ 0.15 %.*

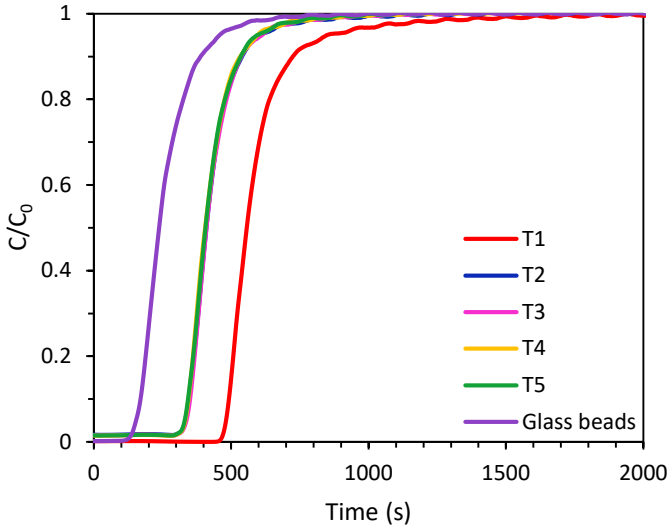


*Figure S7: Cyclic breakthrough curves of LTA beads and glass beads of approximately the same diameter (0.5 mm). LTA beads were regenerated in between cycles by evacuation at 20 mbar for 2 min, followed by flushing with $N_2$ for 139 sec.*

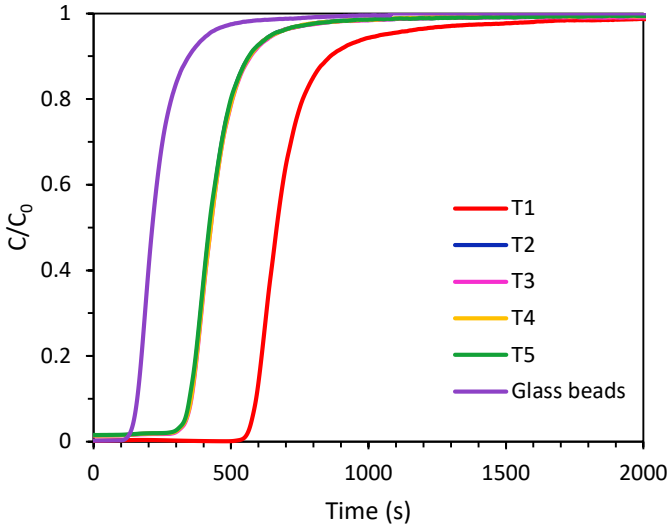


*Figure S8: Cyclic breakthrough curves of the 4A-comm beads and glass beads of approximately the same diameter (3 mm). The 4A-comm beads were regenerated in between cycles by evacuation at 20 mbar for 2 min, followed by flushing with $N_2$ for 139 sec.*

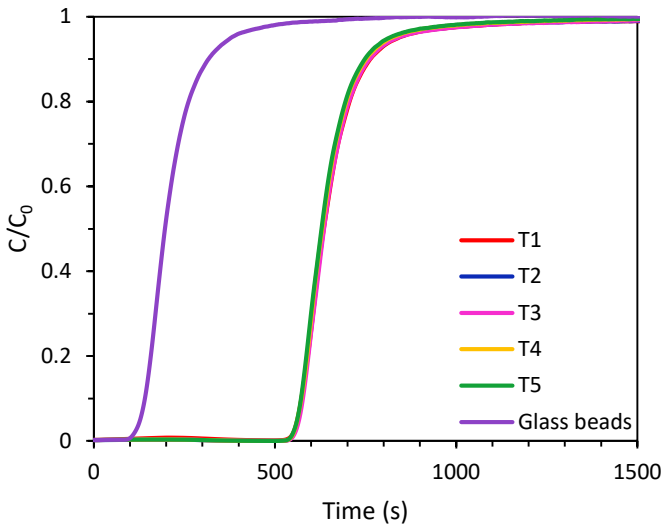


*Figure S9: Cyclic breakthrough curves of SAPO-34 beads and glass beads of approximately the same diameter (1 mm). SAPO-34 beads were regenerated in between cycles by evacuation at 20 mbar for 2 min, followed by flushing with $N_2$ until $CO_2$ concentration ≤ 0.15 %.*

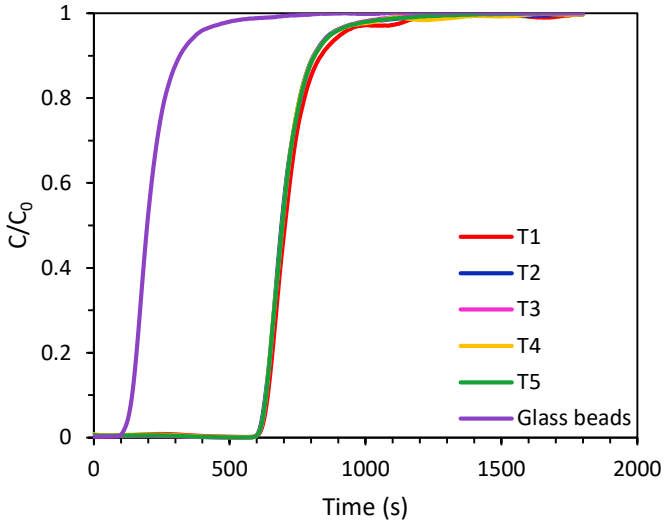


*Figure S10: Cyclic breakthrough curves of SAPO-34 beads and glass beads of approximately the same diameter (1 mm). SAPO-34 beads were regenerated in between cycles by evacuation at 20 mbar for 2 min, followed by flushing with $N_2$ for 139 sec.*

*Table S1: Physicochemical properties of the LTA beads and 4A-comm beads.*

| Adsorbent | BET surface area ($m^2g^{-1}$)[a] | Total pore volume ($cm^3g^{-1}$)[b] | Micropore volume ($cm^3g^{-1}$)[b] | Si/Al ratio | $Na^+$ (mol $g_{bead}^{-1}$) | Relative degree of crystallinity (%) |
|---|---|---|---|---|---|---|
| LTA beads | 160 | 0.18 | 0.05 | 1.61 | 0.234 | 100 (reference material) |
| 4A-comm beads | 38 | 0.11 | <0.01 | 1.25 | 0.27 | 73 |

[a] The BET surface area was obtained by the BETSI software, which applies the Rouquerol criteria to the measured isotherm and uses this to calculate the BET surface area. See Figures S11 and S12 for the Rouquerol plots and the BET transform plots. Note that for the 4A-comm beads enough point were available in the $N_2$ isotherm for applying the Rouquerol criteria and calculate the BET surface area, while for the LTA beads the BET surface area was calculated based on the micropore isotherm measured with Ar. [b] Determined by $N_2$ physisorption.

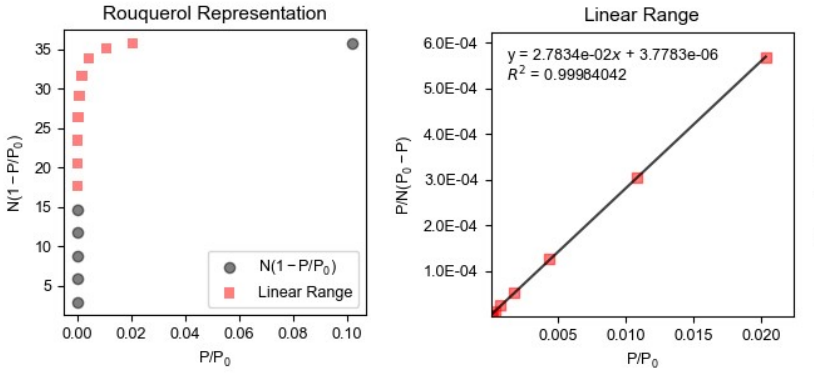


*Figure S11: Rouquerol plot and BET transform plot for the LTA beads.*

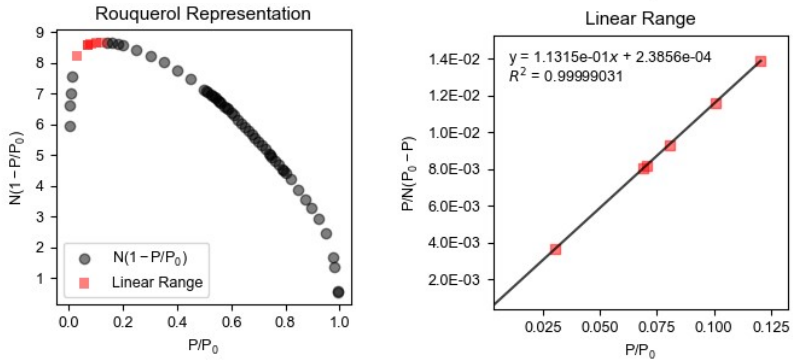


*Figure S12: Rouquerol plot and BET transform plot for the 4A-comm beads.*

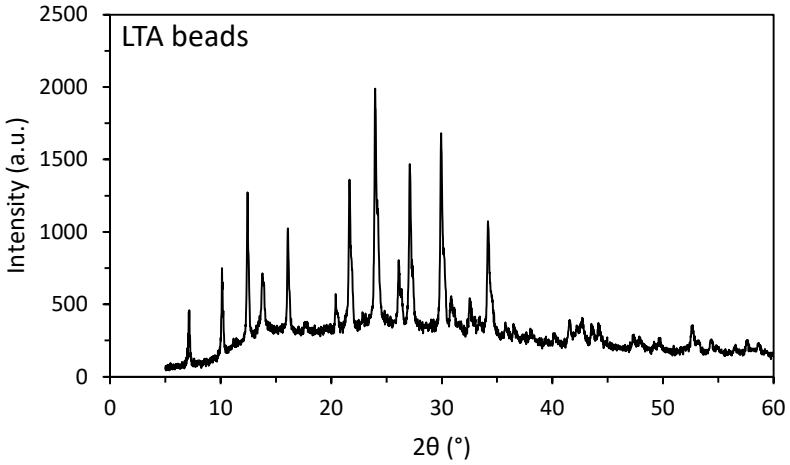


*Figure S13: XRD pattern of the LTA-beads.*

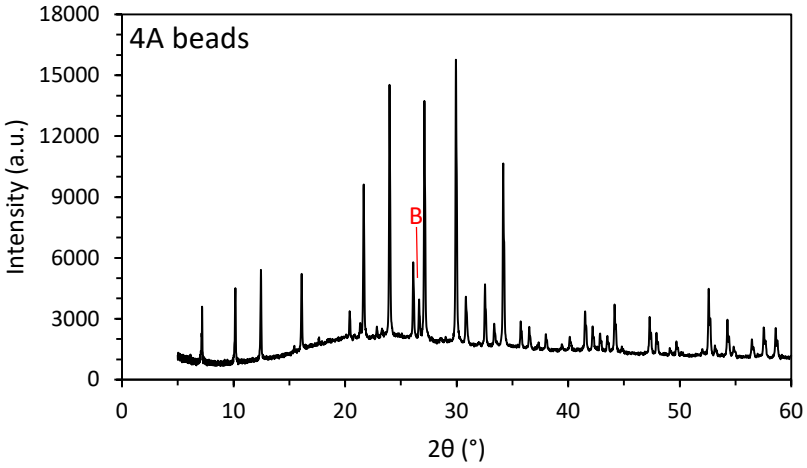


*Figure S14: XRD pattern of the 4A-comm beads. The peak indicated with B does not belong to the LTA framework and likely originates from the binder.*

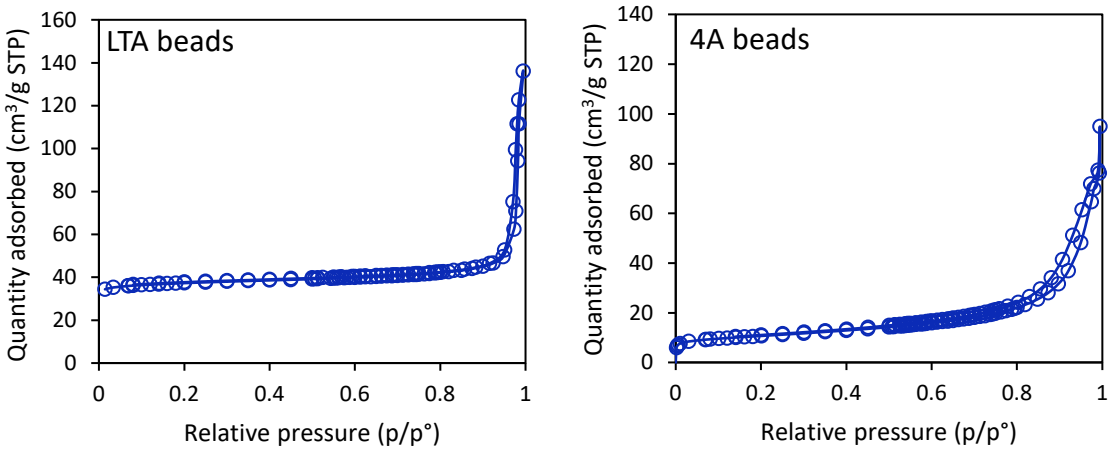


*Figure S15: $N_2$ physisorption isotherms of the LTA beads and 4A-comm beads.*

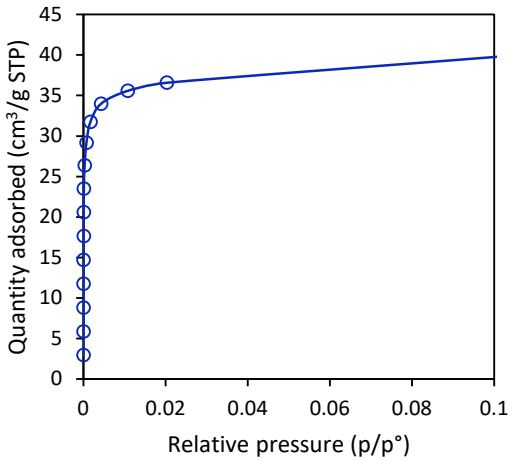


*Figure S16: Ar physisorption isotherm for analysis of the micropores of the LTA beads.*

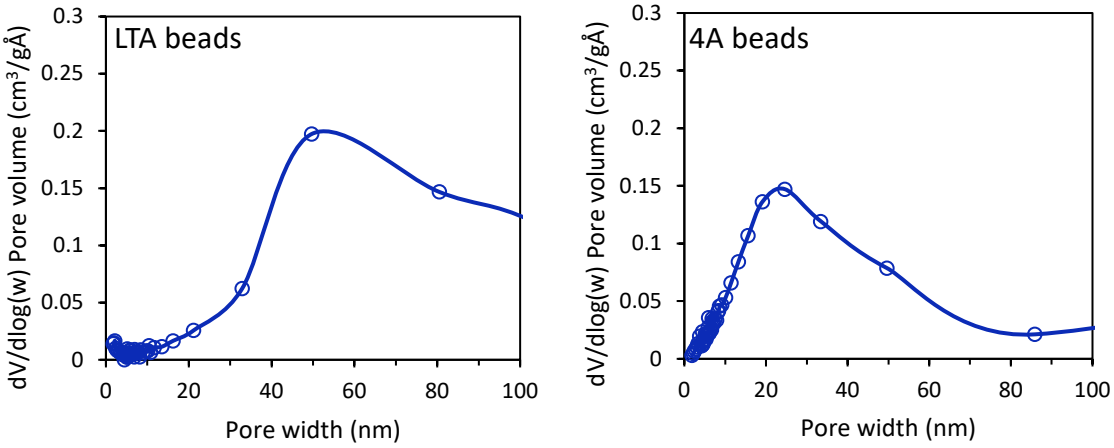


*Figure S17: Pore size distribution of the LTA beads and 4A-comm beads (based on $N_2$ physisorption).*

## Deconvolution of XRD patterns

Deconvolution of the XRD patterns using the Fit Peaks function in OriginPro (as in Figure S18) allowed us to estimate the degree of crystallinity of the beads. For the peaks corresponding to crystalline phases in the beads Lorentzians were selected as peak type to account for peak broadening. For the peaks corresponding to amorphous phases in the beads Gaussians were applied. The parameters were optimized to obtain a good fit of the peaks ($R^2 > 0.96$). The degree of crystallinity was estimated by dividing the sum of the areas corresponding to the crystalline phases by the total area of all peaks (see for example Figure S13). The obtained values are normalized to that of the 4A-comm beads to account for background noise from the sample holder (Table S1, Table S2).

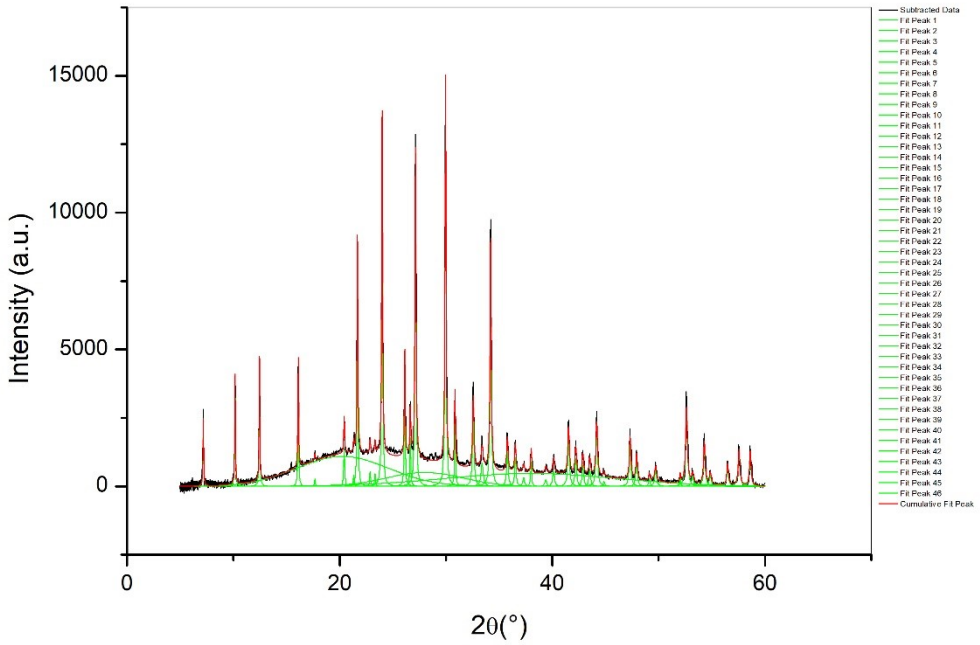


*Figure S18: Deconvolution of the diffractogram of the 4A-comm beads.*

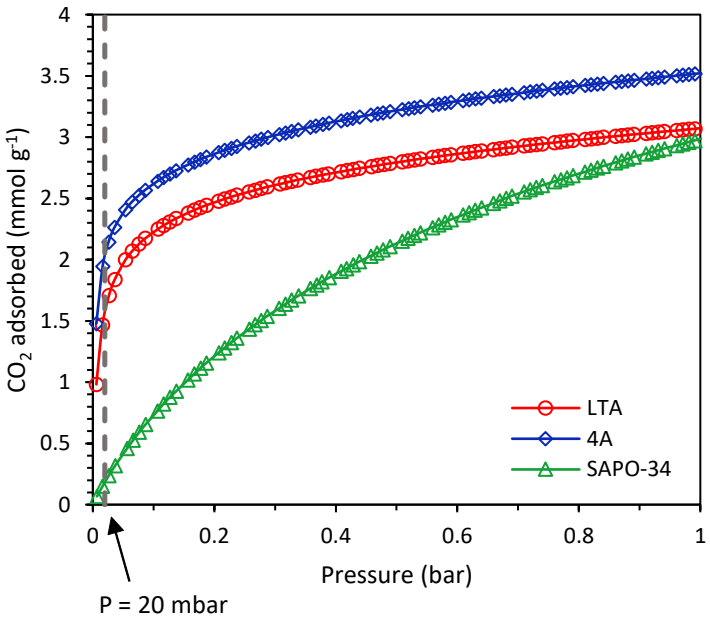


*Figure S19: Single component adsorption isotherm of $CO_2$ for the LTA, 4A-comm and SAPO-34 beads at room temperature. Dashed line signifies the desorption pressure during breakthrough (20 mbar).*

*Table S2: Physicochemical properties of SAPO-34 beads.*

| Adsorbent | BET surface area ($m^2g^{-1}$)[a] | Total pore volume ($cm^3g^{-1}$)[b] | Micropore volume ($cm^3g^{-1}$)[b] | Si/Al ratio | Relative degree of crystallinity (%)[a] |
|---|---|---|---|---|---|
| SAPO-34 beads | 693[b] | 0.38 | 0.24 | 0.28 | 85 |

[a] The BET surface area was obtained by the BETSI software which applies the Rouquerol criteria to the micropore isotherm (measured with Ar) and uses this to calculate the BET surface area. See Figure S20 for the Rouquerol plot and the BET transform plot. [b] Determined by $N_2$ physisorption.[c] Normalized to the crystallinity of the 4A-comm beads, see page 12 for the method used.

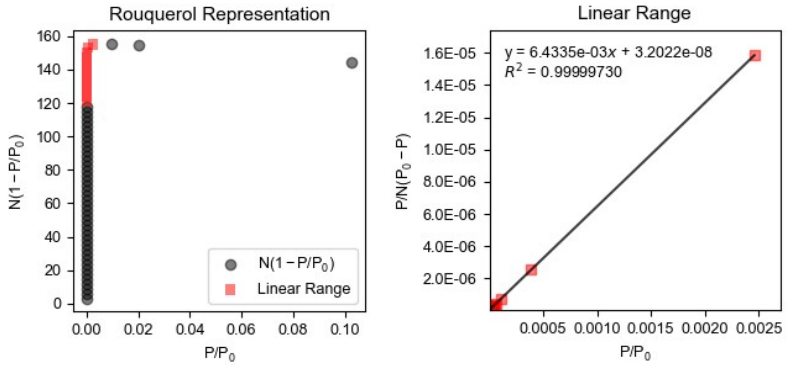


*Figure S20: Rouquerol plot and BET transform plot for the SAPO-34 beads.*

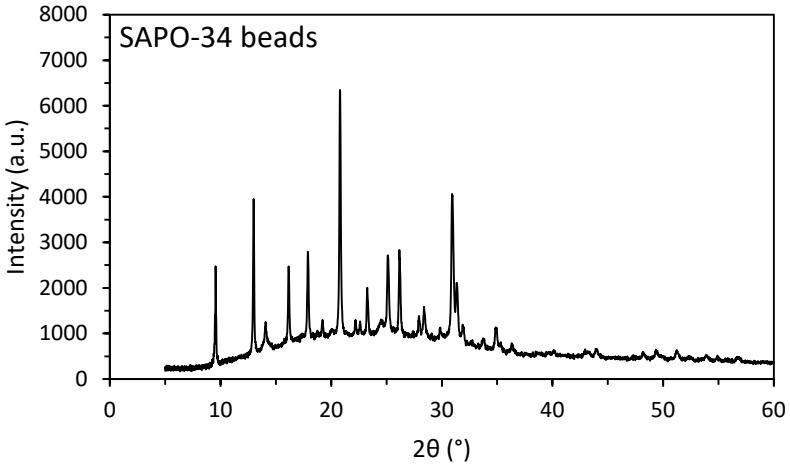


*Figure S21: XRD pattern of the SAPO-34 beads.*

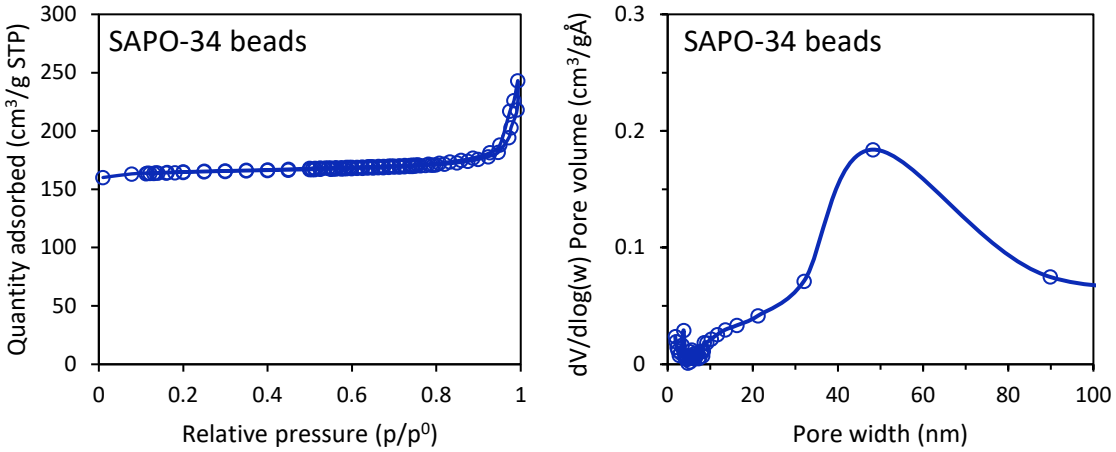


*Figure S22: $N_2$ physisorption isotherm (left) and pore size distribution (right) of the SAPO-34 beads.*

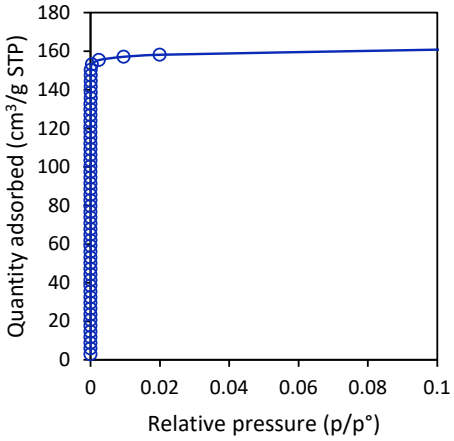


*Figure 23: Ar physisorption isotherm for analysis of the micropores of the SAPO-34 beads.*

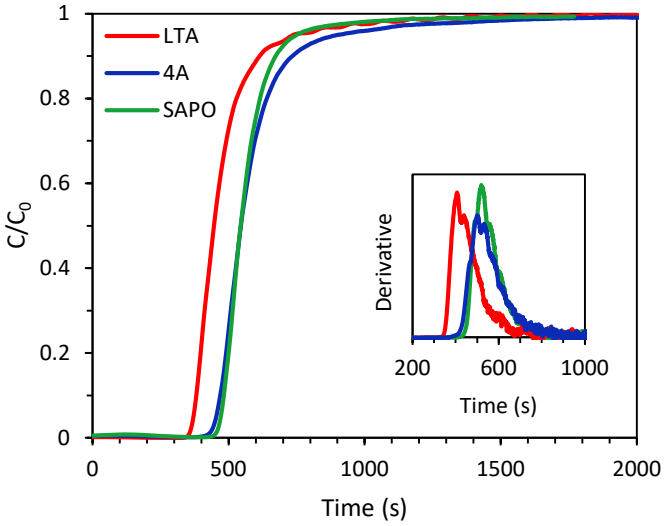


*Figure S24: Breakthrough curves of the LTA, 4A-comm, and SAPO-34 beads. In the inset, the derivative of the breakthrough curves is displayed.*